Automated detection of foveal center in SD-OCT images using the saliency of retinal thickness maps

Sijie Niu[a)]
School of Information Science and Engineering, University of Jinan, Jinan 250022, China
School of Computer Science and Engineering, Nanjing University of Science and Technology, Nanjing 210094, China

Qiang Chen[a)]
School of Computer Science and Engineering, Nanjing University of Science and Technology, Nanjing 210094, China
Fujian Provincial Key Laboratory of Information Processing and Intelligent Control, Minjiang University, Fuzhou 350121, China

Luis de Sisternes
Department of Radiology, Stanford University, Stanford, CA 94305, USA

Theodore Leng
Byers Eye Institute at Stanford, Stanford University School of Medicine, Palo Alto, CA 94303, USA

Daniel L. Rubin
Department of Radiology, Stanford University, Stanford, CA 94305, USA

Purpose: To develop an automated method based on saliency map of the retinal thickness map to determine foveal center in spectral-domain optical coherence tomography (SD-OCT) images.

Methods: This paper proposes an automatic method for the detection of the foveal center in SD-OCT images. Initially, a retinal thickness map is generated by considering the axial distance between the internal limiting membrane (ILM) and the Bruch's membrane (BM). Both the ILM and BM boundaries are automatically segmented by a known retinal segmentation technique. The macular foveal region is identified as a salient feature in the retinal thickness map, and segmented by the saliency detection method based on a human vision attention model. Finally, the foveal center is identified by searching for the lowest point from the determined macular fovea region.

Results: Experimental results in 39 scans from 35 healthy eyes and 58 scans from 29 eyes diagnosed with several stages of age-related macular degeneration (AMD), from mild or intermediate stages to severe dry or wet stages, demonstrated that the proposed method achieves good performance. The mean radial distance error of the automatically detected foveal center locations when compared to consensus manual determination established by repeated sessions from two expert readers was 52 ± 56 μm for the normal eyes and 73 ± 63 μm for AMD eyes.

Conclusions: The proposed algorithm was more effective for detecting the foveal center automatically in SD-OCT images than the state-of-art methods. © *2017 American Association of Physicists in Medicine* [https://doi.org/10.1002/mp.12614]

Key words: foveal center, macular fovea, retinal thickness map, saliency, SD-OCT image

1. INTRODUCTION

The development of spectral-domain optical coherence tomography (SD-OCT) has allowed for advanced noninvasive imaging of intraretinal structures at high resolution, enabling clinicians to rapidly identify possible lesion locations and to measure macular thickness quantitatively. Quantitative measurement of central macular thickness (CMT) is important because it may help clinicians to objectively monitor disease progression[1,2] or make a treatment decision.[3] CMT is measured as the retinal thickness within a 1 mm diameter circle of the Early Treatment Diabetic Retinopathy Study (ETDRs) grid,[4] centered at the fovea pit center, and it has been shown to be closely associated with visual acuity. Macular SD-OCT scans normally cover a region of 6×6 mm of the macula region. As macular thickness can strongly vary when measured at different scan locations, the accurate determination of the foveal center location within the OCT scan plays a vital role in obtaining adequate CMT measurements. Measurement in an inaccurate location within the scan would lead to erroneous CMT values. Manual determination of the foveal center is subject to user-variability, yielding subtle but potentially important differences. A reliable automated approach to identify the foveal center would eliminate such errors.

Currently, there are numerous approaches for automatically detecting the foveal center in color fundus images,[5–17] but few have been described for SD-OCT images (e.g., the postdetection method in the Cirrus HD-OCT software[18]). Most foveal location approaches in color fundus images[5–11] are based on finding the minimum intensity (darker region) within the image and considering the distance from the optic disk to a candidate foveal center while others take advantage

of the vessel density.[12–16] However, such methods are not directly applicable to SD-OCT imaging, as the complexity and sampling of the data acquired are different (two-dimensional in color fundus images versus three-dimensional in SD-OCT) and pathological characteristics that may be exploited for the fovea center location appear differently in the two imaging techniques.

The pathological characteristic of the foveal center in SD-OCT images of an average healthy eye is the lowest point (highest axial depth) in the foveal depression on both horizontal and vertical planes (as shown in Fig. 1), and this characteristic is normally taken as the key feature in fovea center determination.[18] Previous studies[18–21] have reported that automated postdetection of the foveal center improves the measurement of macular thickness using the Cirrus HD-OCT software, although specific details for this method are not publicly available. Several intraretinal segmentation algorithms[22–24] also proposed their own simple foveal center determination method by searching the minimum thickness between the different layers. However, irregularity in retinal structures or the presence of disease can cause thinning and loss in isolated regions of different retinal layers, altering the internal limiting membrane (ILM) depth locally and limiting the ability of previous methods to identify the foveal center for both normal eyes and diseased eyes. Additional difficulties are derived from possible eye tilting or incorrect alignment in the acquired images. Due to the above limitations, a simple algorithm relying on finding the local minimum point within the ILM surface or simply searching for the smallest distance between different layers would not be a robust approach to accurately determine the position of foveal center. Taking into consideration the saliency of the full retinal thickness and assuming that the foveal depression should present a localized region of thinning in the macula can improve the detection of the foveal center. Full retina thickness maps can be generated by considering the axial distance between the ILM and the Bruch's membrane (BM). Although disease can also affect such topographic maps, foveal center detection seems relatively more robust by including such considerations rather than adopting a simple algorithm based on finding the minimum ILM to BM distance.

The foveal center, being located at the foveal depression, can be recognized as saliency of the retinal thickness map, as shown in Fig. 1(e), which can provide a key feature for its automatic detection. In computer vision,[17,25] saliency detection has been widely studied in a variety of nonmedical applications for object recognition,[26] image quality assessment,[27] video summarization,[28] and other applications.[29,30] Compared with traditional regional segmentation methods, saliency detection methods utilize a human vision attention model for detecting a salient object. Several methods have been proposed to extract saliency information, including "center-surround" difference,[28] graph-based visual saliency,[31] spectral residual-based saliency detection,[32] Bayesian probabilistic framework,[33,34] global contrast-based salient region detection,[35] and partial differential equation learning for saliency detection.[36] Modern methods[37,38] are based on a non-parametric estimation of the likelihood of saliency,
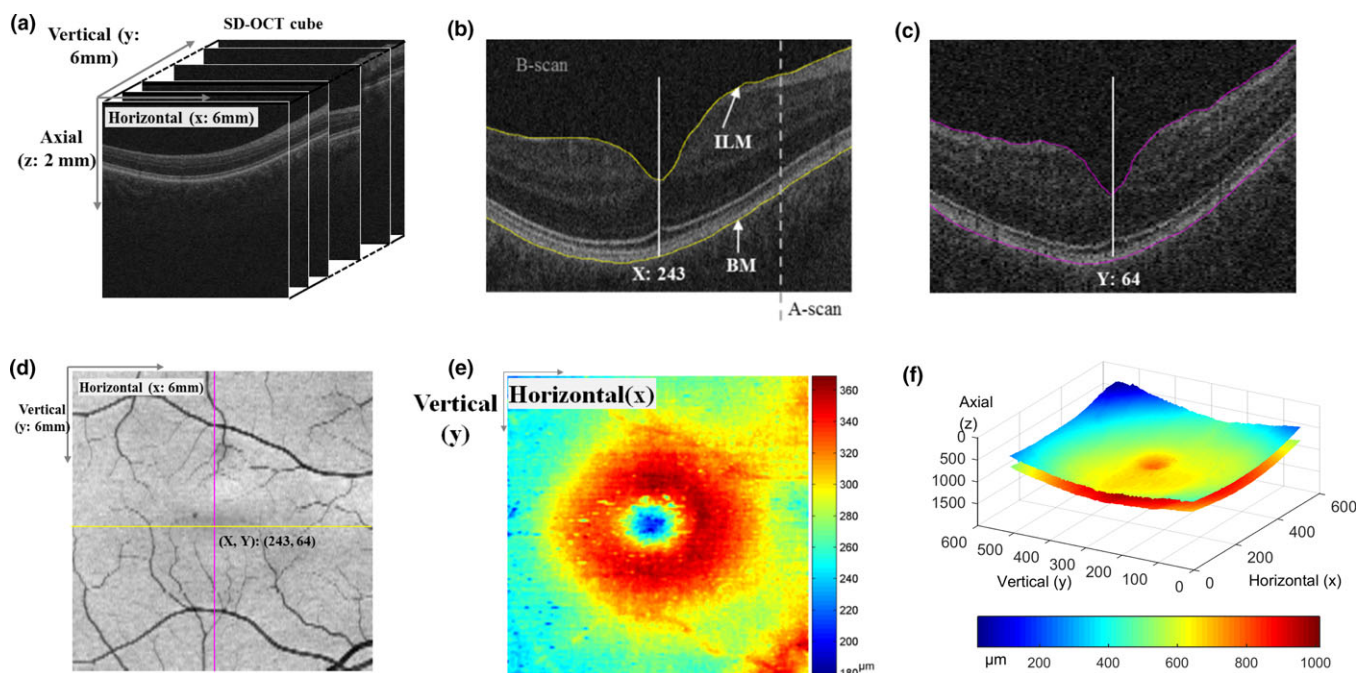

Fig. 1. Location of the fovea center in example SD-OCT data. (a) Representation of 3D SD-OCT cube data. The fovea center is identified in the lowest point of fovea depression on both the horizontal scan (b) and the vertical scan (c). The y direction represents a B-Scan location; x direction represents an A-Scan within the B-scan; z direction represents axial depth. (d) Summed projection of 3D OCT data along the axial direction. (e) Retina thickness map as distance from ILM to BM. (f) 3D representation of ILM and BM surfaces in OCT data. The color bar indicates axial depth with respect to the innermost location in the data.[Color figure can be viewed at wileyonlinelibrary.com]

employing local steering kernels as features, which extract local data structure information exceedingly well and accurately detect salient objects from images without any background knowledge. Although the current methods[37,38] present some advantages, defects related to retinal disease and potential errors in layer segmentation (a necessary pre-processing step to determine retinal thickness) can affect saliency detection and produce erroneous determination when directly applied to retinal thickness maps. The main reason for these difficulties is that only local steering kernels are taken as features for detecting an object within the images. On the other hand, orientation features and location information should also be important when generating a saliency map in topographic retinal images produced from SD-OCT data. An improved method with local orientation feature and location information, similarly as used in "feature integration theory",[29] is proposed here to overcome these difficulties.

In this work we introduce a novel algorithm for detecting the foveal center in SD-OCT images using saliency of the retinal thickness map and we evaluate it in healthy eyes and in eyes with mild to severe age-related macular degeneration (AMD) — a challenging problem not solved to date. The key idea is to search for the lowest point within the foveal region segmented by a modified saliency detection method.

2. METHODS

The proposed method searches for the foveal depression region in the retinal thickness map to identify the foveal center. An overview of the proposed approach is shown in Fig. 2. In order to produce the retinal thickness map, the axial location of the ILM and BM are first estimated for all locations in a horizontal/vertical plane by an automated layer segmentation method.[22] The depression region can be seen in the thickness map as the location of reduced thickness surrounded by regions of increased thickness, increasing visibility and human visual attention, as shown in Fig. 1(e). This foveal region is segmented by an improved saliency detection method and the foveal center is then identified by finding the lowest point of depression within such region.

2.A. Retinal layer segmentation

The location of multiple intraretinal boundaries within the SD-OCT image can be determined using an automated retinal layer segmentation method, allowing a posterior quantitative analysis of axial thickness between different boundaries.
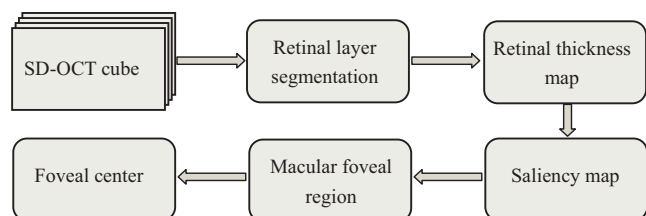

FIG. 2. The overview of the foveal center identification method. [Color figure can be viewed at wileyonlinelibrary.com]

Here, a total retina thickness map is produced by measuring the axial distance between BM and ILM as shown in Fig. 1(e). The axial position of both boundaries is automatically estimated by employing a previously published segmentation method.[22]

2.B. Saliency map detection

We identify the fovea depression region by employing an improved saliency detection method. The method includes improvements made in local orientation features, local data structure features and location information, similar to those in "feature integration theory".[28] Orientation feature captures the orientation information within local neighborhoods. Local data structure feature considers the data similarity between a center pixel and its neighborhood pixels. Location feature locates the salient region at the center of the image. An overview and image example with advanced dry AMD (i.e., geographic atrophy) is shown in Fig. 3. Three saliency feature images are computed (orientation feature, local data structure feature, and location feature), which later contribute to the computation of the saliency map.

2.B.1. Extraction of orientation feature

Given the location of pixel i, indicated by $\varphi_i \in [X, Y]$, where $i = 1, 2, \cdots M$, and M is the total number of pixels in the given image, X and Y are the coordinates on the horizontal and vertical directions, respectively, the orientation feature is extracted from the retinal thickness image $I(\varphi_i)$ using oriented Gabor pyramids $O(\sigma, \theta, \varphi_i)$, where $\sigma \in [0, 1, \cdots 8]$ denotes the scales and $\theta \in \{0^o, 45^o, 90^o, 135^o\}$ represents the orientation.[39] The orientation feature is detected from the input image using a center-surround differences strategy as proposed by Itti et al.[28] The across-scale differences between a "center" location at scale $c \in \{2, 3, 4\}$ and a "surrounding" location at scale $s = c + \delta$, with $\delta \in \{3, 4\}$ are computed for each input image as follows:

$$\vartheta(c, s, \theta, \varphi_i) = |\mathrm{O}(c, \theta, \varphi_i) - \mathrm{O}(s, \theta, \varphi_i)| \quad (1)$$

The orientation feature map $S_O(\varphi)$ is then computed by combining the results of the six possible across-scale differences for a given orientation θ, and subsequent combination for a set of the four different orientations. For a particular pixel location φ_i:

$$S_\mathrm{O}(\varphi_i) = \sum_{\theta \in \{0^o, 45^o, 90^o, 135^o\}} \sum_{c=2}^{4} \sum_{s=c+3}^{c+4} N(\vartheta(c, s, \theta, \varphi_i)) \quad (2)$$

where $N(\vartheta(c, s, \theta, \varphi_i))$ is a function defined to normalize the center-surround differences as in the reference.[28]

2.B.2. Extraction of local data structure feature

As similarly done by Hae Jong Seo et al.[37,38] for detecting the local saliency map, we categorize each pixel position φ_i
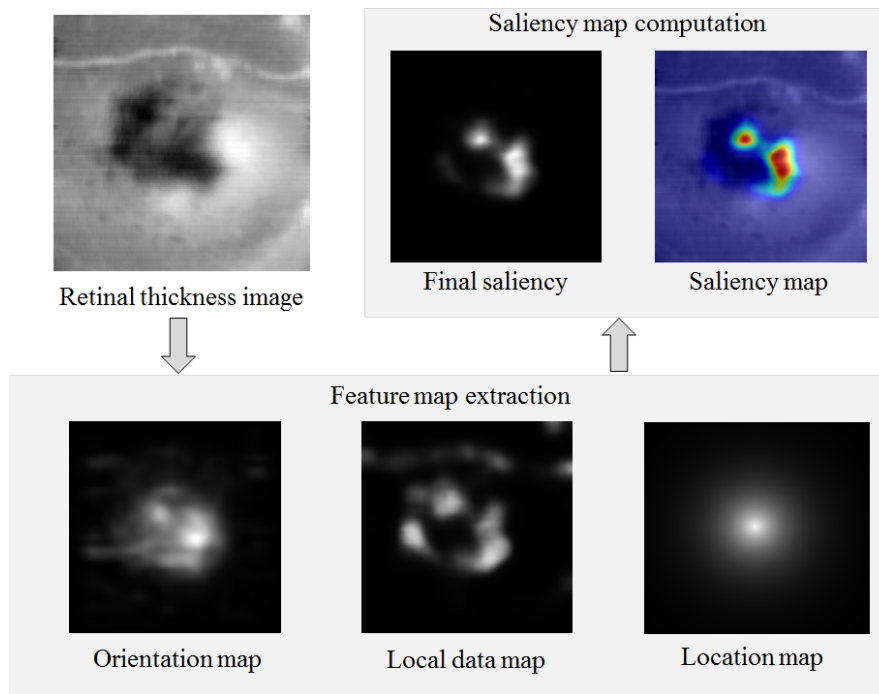
FIG. 3. The proposed saliency map detection method. Red values in saliency map represent higher saliency while blue values denote lower saliency. [Color figure can be viewed at wileyonlinelibrary.com]

in the given image using a saliency mask (describing whether a pixel is salient or not) as follows:

$$Sm_i = \begin{cases} 1 & \text{if } \phi_i \text{ is salient} \\ 0 & \text{otherwise} \end{cases} \tag{3}$$

The local data structure feature at a pixel position φ_i is defined by the posterior probability with respect a given feature set:

$$S_D^i = \Pr(Sm_i = 1 | F) \tag{4}$$

where $F = [F_{N-i}, \ldots, F_{i+N}]$ indicates a feature set defined as a matrix of feature vectors obtained not only from the center pixel location but also from a surrounding region. N indicates the width of feature vectors considered around the center pixel φ_i. $F_i = [f_i^1, \cdots, f_i^L]$ is the feature vector collected in a local window centered at the pixel location φ_i, with L being the number of pixels contained in such local window. For a square local window of size 5×5 (as used in the experiments presented here) centered at the location φ_i, the feature vector would be $F_i = [f_i^1, \cdots, f_i^{25}]$.

The feature vector F_i is extracted using the local steering kernel function $K(\varphi_l - \varphi_i)$. In practice, this function is calculated at every pixel location and normalized as follows:

$$f_i^l = \frac{K(\varphi_l - \varphi_i)}{\sum_{l=1}^{L} K(\varphi_l - \varphi_i)}, i = 1, \cdots M; l = 1, \cdots, L \tag{5}$$

$$K(\varphi_l - \varphi_i) = \frac{\sqrt{\det(C_l)}}{h^2} \exp\left(-\frac{(\varphi_l - \varphi_i)C_l(\varphi_l - \varphi_i)'}{2h^2}\right) \tag{6}$$

where h is a global smoothing parameter (assigned as 0.2 in the experiments presented here) and the matrix C_l ($C_l \in R^{2 \times 2}$) is a Hessian matrix of size 2×2 defined from the collection of gradients within the local window centered at a position φ_l.

According to the Bayes' theorem, Eq. (4) can be rewritten as:

$$S_D^i = \frac{p(F | Sm_i = 1)p(sm_i = 1)}{p(F)} \tag{7}$$

Without any prior knowledge, we can consider that the saliency probability of a given pixel follows a uniform distribution (pixels are equally likely to be salient given no information about them). The probability $p(F)$ can also be written as $p(F) = p(F | Sm_i = 1)p(Sm_i = 1) + p(F | Sm_i = 0)p(Sm_i = 0)$. Therefore, Eq. (7) indicates that saliency is mainly proportional to the conditional probability $p(F | Sm_i = 1)$. As in previous work,[40,41] a kernel can be employed to estimate such probability, using a center value of normalized adaptive kernel $G(\cdot)$ to estimate it at a pixel position φ_i:

$$S_D(\varphi_i) \propto p(F | Sm_i = 1) = \frac{G_i(\overline{F}_i, \overline{F}_i)}{\sum_{j=1}^{N} G_i(\overline{F}_i, \overline{F}_j)} \tag{8}$$

where $G_i(\overline{F}_i, \overline{F}_j) = \frac{1}{2\pi\sigma_D} \exp\left(\frac{-\|\overline{F}_i - \overline{F}_j\|_2^2}{2\sigma_D^2}\right)$, $\overline{F}_i = \left[\frac{f_i^1}{\|F_i\|_2}, \cdots \frac{f_i^L}{\|F_i\|_2}\right]$, and σ_D is a control parameter.

Inspired by the earlier studies,[42,43] the kernel function G_i can be rewritten by using the concept of matrix cosine similarity[42] as:

$$G_i(\overline{F}_i, \overline{F}_j) = \frac{1}{2\pi\sigma_D} \exp\left(\frac{-1 + \rho(F_i, F_j)}{\sigma_D^2}\right) \tag{9}$$

where $\rho(F_i, F_j)$ is the matrix cosine similarity between two normalized feature matrices $\overline{F}_i, \overline{F}_j$, defined as the "Frobenius inner product" between normalized features matrices $\rho(F_i, F_j) = <\overline{F}_i, \overline{F}_j>$. This similarity matrix can be rewritten as a weighted sum of the standard cosine similarity $\rho(F_i, F_j) = \sum_{l=1}^{L} \frac{f_i^l}{\|F_i\|_2} \frac{f_j^l}{\|F_j\|_2}$, with the detailed derivation found in 37,38. Considering Eqs. 8 and 9, and the fact that $\rho(F_i, F_i) = 1$ and therefore $G_i(\overline{F}_i, \overline{F}_i) = \frac{1}{2\pi\sigma_D}$, the local data structure feature map at a pixel position φ_i is determined as follows:

$$S_D(\varphi_i) \propto \frac{G_i(\overline{F}_i, \overline{F}_i)}{\sum\limits_{j=1}^{N} G_i(\overline{F}_i, \overline{F}_j)} = \frac{1}{\sum\limits_{j}^{N} \exp\left(\frac{-1 + \rho(F_i, F_j)}{\sigma_D^2}\right)} \tag{10}$$

The normalized kernel function $G(\cdot)$ depicts the local structure of images by analyzing pixel similarity between center pixel φ_i and the surrounding pixel in a local window, which is achieved by using a local steering kernel. As shown in Eq. (10), the estimated probability density (i.e., $S_D(\varphi_i) \propto p(F|Sm_i = 1)$) reveals how salient a pixel is, considering the similarity between its neighborhood features F_i and the surrounding feature matrices F_j. A high probability density indicates that the pixel position φ_i presents a high salient.

2.B.3. Extraction of location feature

In a retinal thickness map, the macular fovea is normally near the center of the image $I(\varphi)$, which is more conspicuous to human attention. We use a Gaussian distribution to estimate the location feature at every pixel position φ_i:

$$S_L(\varphi_i) = \frac{1}{\sqrt{2\pi}\sigma_L} \exp\left(-\frac{\|\varphi_i - ic\|^2}{2\sigma_L^2}\right) \tag{11}$$

where ic is the coordinates center of the given image and σ_L is a control parameter.

2.C. Saliency map computation

The orientation feature, local data structure feature and location feature are normalized (taking values within the interval [0 1]) and multiplied pixel-by-pixel to form the final saliency maps:

$$S(\varphi) = S_O(\varphi) \cdot S_D(\varphi) \cdot S_L(\varphi) \tag{12}$$

where S_O, S_D and S_L indicate the orientation saliency, local saliency, and location saliency maps, respectively, and the product indicates pixel-by-pixel multiplication.

2.D. Identification of the foveal center

A foreground saliency region is segmented by thresholding the saliency map obtained in the previous subsection. The mean value recorded in the saliency map is taken as a threshold *th*, and the foreground saliency region is determined as follows:

$$MSK(\varphi_i) = \begin{cases} 1 & if\ S(\varphi_i) > th \\ 0 & otherwise \end{cases} \tag{13}$$

MSK represents a mask where the saliency region is presented (example shown in Fig. 4(a)). The foveal center is identified by searching the location of minimum total retina thickness within the foreground saliency region as follows:

$$P = \arg \min_{\varphi_i \in \{MSK(\varphi_i) = 1\}} \{RTM(\varphi_i)\} \tag{14}$$

where $RTM(\varphi)$ is the retinal thickness map. Figure 4(a) shows an example foreground saliency region with the identified foveal center indicated with a red dot. Figure 4(b) shows the identified foveal center on the retinal thickness image.

3. RESULTS

3.A. Experimental data and evaluation studies

Our algorithm was implemented in Matlab (The MathWorks, Inc.) and run on a 2.16 GHz Pentium Dual PC with 3 GB RAM memory. Each foveal center computation in an
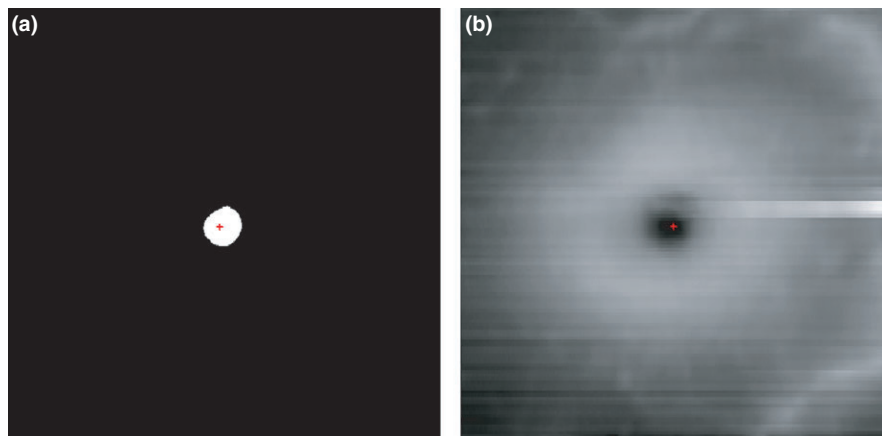

FIG. 4. The foveal center (shown as a red dot) and macular central fovea region detected by the proposed method. (a) Binary masked saliency image with foveal center; (b) Foveal center on the retinal thickness image. [Color figure can be viewed at wileyonlinelibrary.com]

OCT cube took approximately 10 s. Two datasets were compiled to validate the proposed method. The first longitudinal dataset is used to tune the parameters, including 13 SD-OCT cubes from 13 healthy eyes and 57 SD-OCT cubes from 41 eyes having different stages of severity in age-related macular degeneration (AMD): 6 scans (2 eyes) diagnosed with intermediate AMD, 30 scans (18 eyes) diagnosed with advanced dry AMD (presence of geographic atrophy), 15 scans (15 eyes) diagnosed with diabetic and no diabetic retinopathy, and 6 scans (6 eyes) diagnosed with nonproliferative diabetic retinopathy. We tested our algorithm by compiling the second longitudinal dataset that included 39 SD-OCT cubes from 35 healthy eyes and 58 SD-OCT cubes from 29 eyes having different stages of severity in age-related macular degeneration (AMD): 4 scans (3 eyes) diagnosed with mild AMD, 11 scans (8 eyes) diagnosed with intermediate AMD, 32 scans (7 eyes) diagnosed with advanced dry AMD (presence of geographic atrophy), 2 scans (2 eyes) diagnosed with advanced wet AMD (evidence of choroidal neovascularization), 2 scans (2 eyes) diagnosed with diabetic and no diabetic retinopathy and 7 scans (7 eyes) diagnosed with nonproliferative diabetic retinopathy.

All eyes were scanned with a Cirrus SD-OCT device (Carl Zeiss Meditec, Inc., Dublin, CA, USA) by a single experienced technician who was certified by an image reading center for OCT imaging. The scanned area covered a 6×6 mm^2 area on the retina, and the scanning macular protocol was a $1024 \times 512 \times 128$ raster scan (corresponding to $2 \times 6 \times 6$ mm^3 volume). When acquiring the SD-OCT data, the scan location was centralized in the macula region and these scan centers may deviate the actual foveal center. The operator later adjusted the scan center manually if necessary.

The relative position of the foveal center in each SD-OCT dataset was represented in X and Y coordinates based on a 512×128 sampling grid (the SD-OCT cubes were acquired with 512 and 128 A-scans in the horizontal and vertical directions, respectively). The foveal center in each cube was manually identified by two different specialists in two repeated separate reading sessions. The repeated sessions were separated by roughly a week interval so as to eliminate any prior knowledge of the images in the set. The specialists identified the A-scan location of the lowest point of the foveal depression in the ILM boundary within the B-Scan that more clearly showed such depression, visually scanning the B-scans throughout each SD-OCT cube. $R_{i,j}$ represents the foveal center location as identified by the ith reader in the jth session, while we employ R to represent an established consensus location between readers and session, computed as described previously[19,44] and taken as the gold standard in our evaluation. The location of the foveal center was also detected by our proposed algorithm and labeled as AC. The label SC indicates the location of the geometric scan center, which coordinates were (256, 64) in our dataset. For those advanced AMD scans where the original Cirrus data were available (24 scans), we also collected the fovea center location automatically detected

by Cirrus HD software (version 6.0.2.81) for comparison (labeled as *Cirrus*).

We used two different criteria in the evaluation of the proposed algorithm: (a) quantification of the possible discrepancies found in the manual identification results by different specialists (interobserver agreement) and by the same specialist in the two repeated sessions (intraobserver agreement); (b) a comparison of the differences between different methods (e.g., automated method (AC), geometric scan center (SC), Cirrus HD-OCT software ($Cirrus$)) and manual identification results (R) with the measured observed interobserver and intraobserver agreements.

We employ three metrics to assess the differences between pairs of the detection methods: Signed differences of X and Y coordinates ($xdif$ and $ydif$, respectively) and the radial distance (RD)

$$xdif(i,j;k) = x_k^i - x_k^j \tag{15}$$

$$ydif(i,j;k) = y_k^i - y_k^j \tag{16}$$

$$RD(i,j,k) = \sqrt{\left(x_k^i - x_k^j\right)^2 + \left(y_k^i - y_k^j\right)^2} \tag{17}$$

where x_k^i and x_k^j indicate X coordinates in the k-th scan detected by the methods i and j, respectively. y_k^i and y_k^j indicate Y coordinates in the k-th scan detected by the methods i and j, respectively.

3.B. Parameters evaluation

We tuned the parameters employed in our method by examining the mean radial distance across scans in the first dataset as we varied their values, with results shown in Fig. 5. For σ_D and σ_L, we experimented with values ranging from 0.1 to 1 and from 1 to 10, respectively. Figure 5(c) displays mean radial distance as a function of these two parameter values, where L, N, and h were set up to 5, 5, and 0.4, respectively. σ_D had relatively limited influence on performance for the ranges examined, while σ_L seemed to produce adequate results with values 5. Consequently, σ_D and σ_L were set up to have values of 0.4 and 5, respectively. We also varied the values of size of feature vector and local window from 3 to 9 in increment steps of 2 to test their influence. Figure 5(b) indicates these two parameters had limited influence on performance. Overall, adequate performance was achieved with the choice of $L = 5 \times 5$ and $N = 5 \times 5$. Figure 5(a) displays the mean radial distance as the global smoothing parameter h varies from 0.1 to 1 with increments of 0.1. We observed that an adequate performance for a value of 0.2, which was assigned for the experiments.

3.C. Qualitative evaluation

Figures 6 and 7 display examples of foveal center determined by our automated method (white) and reader (yellow) in healthy eyes and AMD eyes, respectively. The cases

displayed in Fig. 6 show the relative simplicity of determining the fovea center in healthy eyes. The AMD eye examples displayed in Fig. 7 show cases with increasing levels of disease status and complexity, with higher disruptions in the normal layer appearance. We can observe in the third and

fourth row of Fig. 7 that the disease notably disrupted the axial location of the ILM, which would present a challenge identifying the foveal center for most known methods. It can be seen from Fig. 7 the proposed method was able to estimate the precise foveal center.
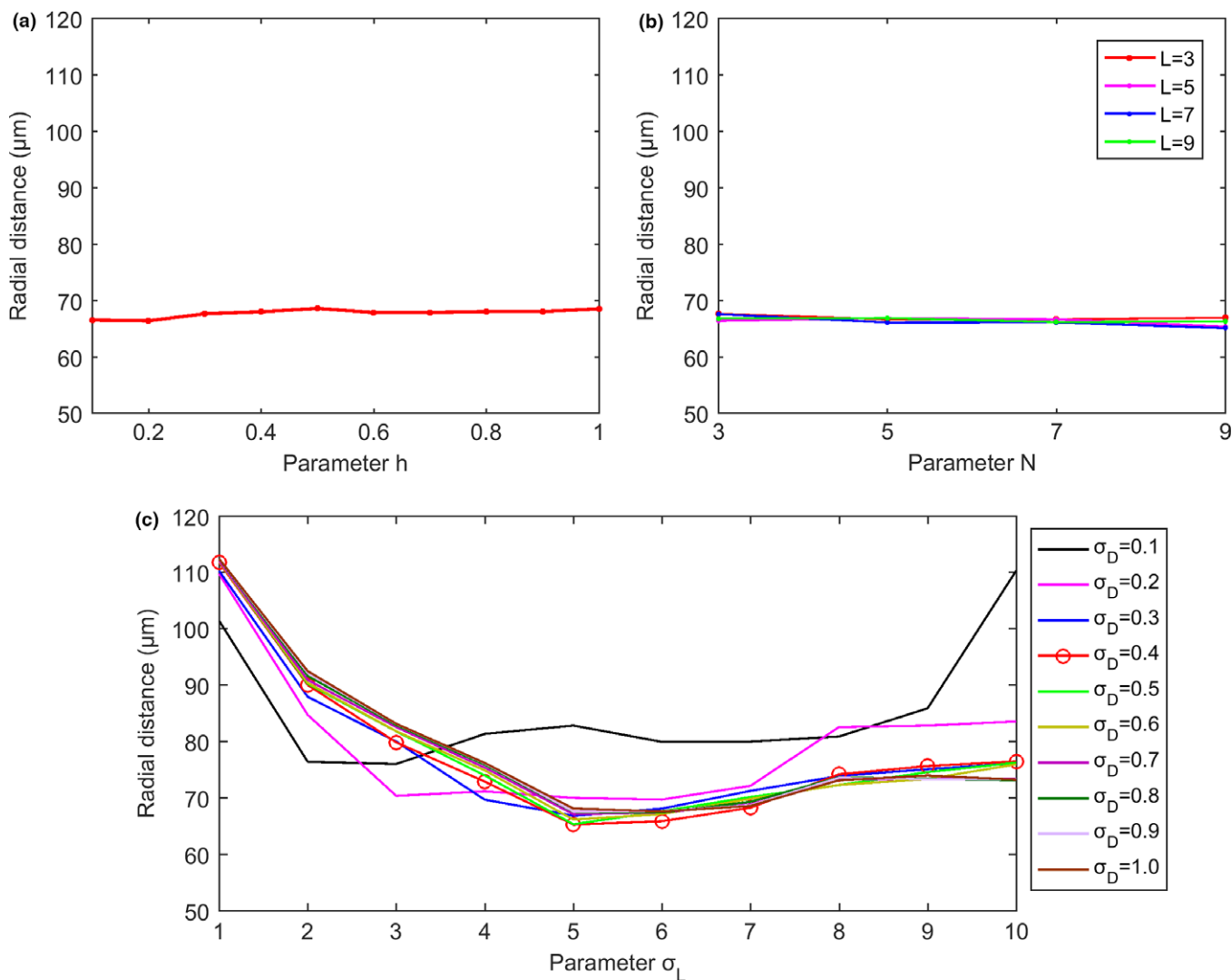
FIG. 5. Mean radial distance for the parameter selection of the proposed method. (a) Mean radial distance for the selection of smoothing parameter h. (b) Mean radial distance for different L and N values. (c) Mean radial distance for different σ_D and σ_L values. [Color figure can be viewed at wileyonlinelibrary.com]
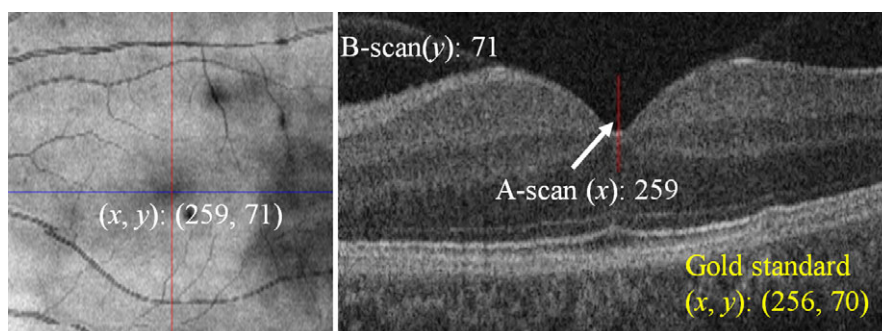

FIG. 6. Examples displaying the automatically detected foveal center location on SD-OCT fundus images (left column) and B-scan images (right columns) in normal eyes. [Color figure can be viewed at wileyonlinelibrary.com]
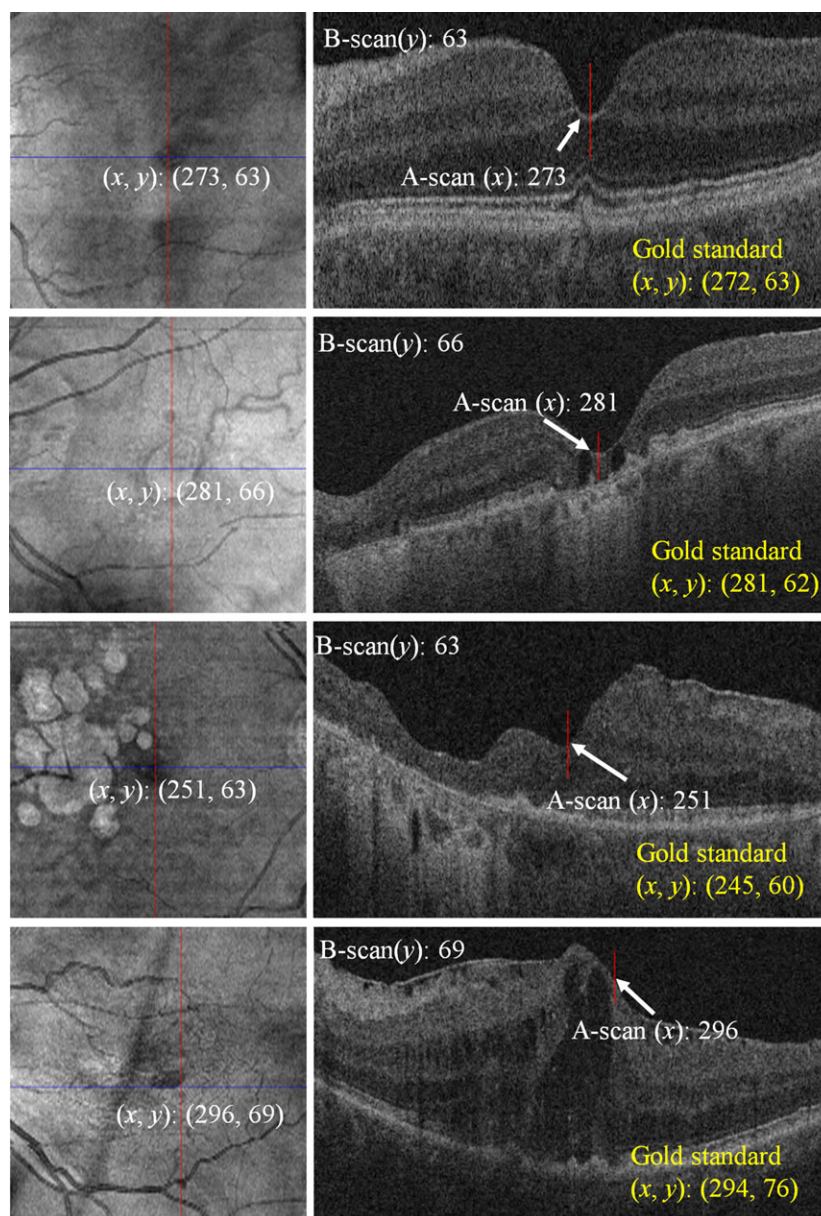
FIG. 7. Results of the automated foveal center detection on examples with AMD. The left column and right column are SD-OCT fundus images and B-scan images, respectively. The first row shows the results in a mild AMD example, the second and third row show the results in advanced dry AMD examples (with geographic atrophy (GA)), and the fourth row shows the results in an eye with advanced wet AMD. [Color figure can be viewed at wileyonlinelibrary.com]

3.D. Quantitative evaluation

Bland–Altman plots[45] were used to assess intraobserver and interobserver agreement. The analysis was performed separately for the X and Y coordinates of foveal center locations. Figures 8 and 9 display the Bland–Altman plots for intra- and interobserver differences (in microns) for healthy eyes and eyes with AMD, respectively. For normal eyes, differences produced by manual identification of two different readers presented a slightly higher level of agreement than those produced by each specialist at two separate sessions, as shown in Fig. 8, which may be an effect of the inevitable error when making repeated manual annotations. On the other hand, the interreader differences in the X coordinate

were higher than those observed at separate sessions from the same specialist in eyes with AMD, but such differences were comparable. Y coordinate intrareader agreement was similar for the two readers and for both normal eyes and AMD eyes, while differences were higher than compared to the X coordinate. The reason is that 128 horizontal B-scans (Y coordinate) are taken in a span of 6 mm while 512 A-scan in each horizontal B-scan (X coordinate) are taken in a span of 6 mm. It is important to note that the differences are displayed in micron units, and the interreader agreements in both X and Y coordinates are similar for both normal eyes and AMD eyes (128 horizontal B-scans taken in a span of 6 mm versus 512 A-scan in each horizontal B-scan taken in a span of 6 mm). We also observed very high correlation in
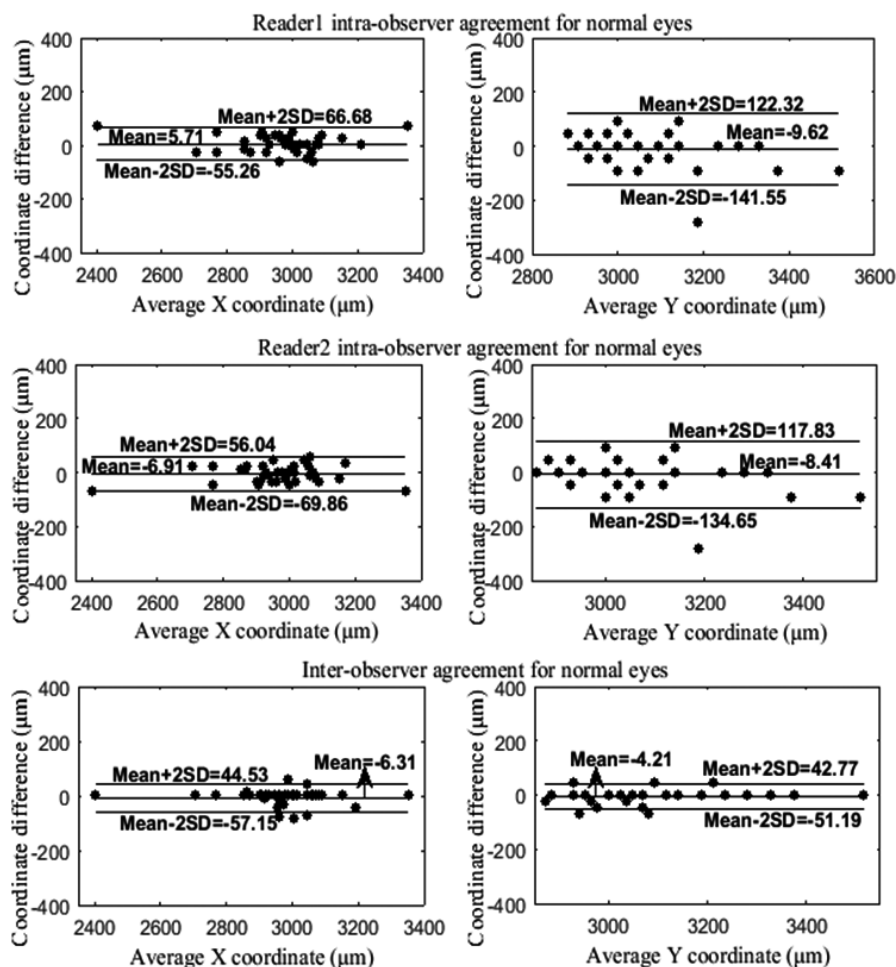
FIG. 8. Bland–Altman plots of intraobserver agreement and interobserver agreement for normal eyes, where the top, middle, and bottom horizontal lines are Mean+2SD, Mean, and Mean-2SD, respectively. The first and second columns display the Bland–Altman plots for the *X* and *Y* center coordinates, respectively.

both the *X* and *Y* foveal center coordinates as identified by the two different manual readers (interobserver differences) or by each reader at separate sessions (intraobserver differences), all with Pearson's correlation coefficients higher than 0.9. The foveal center location differences in *X* and *Y* coordinates for the two different manual readers and for each reader at separate sessions showed no statistical significance, presenting very high *P*-values in a *U*-test (all with $P > 0.05$).

Table I summarizes the radial distance measurements in normal eyes and AMD eyes between the two observers, between each observer at separate sessions, between the gold standard (*R*) and scan center (*SC*), and between R and our proposed automated method (*AC*). Additionally, we also compared the radial distance results between *R* and two additional foveal center determination methods: as generated by finding the saliency map of the deepest depression region from the ILM surface (ILM algorithm), and as generated by searching the smallest distance between ILM and BM (ILM-BM algorithm[23,24]). The radial distances between our automated method and the gold standard for both normal eyes and eyes with AMD was smaller in average than those between *SC* and *R*, between ILM algorithm and *R*, and

between ILM-BM algorithm and *R*, but slightly higher than those observed between the readers. One of the main reasons for the larger difference is that irregularity in retinal structures or the presence of disease can cause thinning and loss in isolated regions of different retinal layers, limiting the ability of previous methods to identify the foveal center for both normal eyes and diseased eyes. These comparison results demonstrate that the proposed method provides accurate and robust identification. Figure 10 displays the Bland–Altman plots of differences between *R* and *AC* for the *X* and *Y* coordinates of the determined foveal centers for the normal and AMD eyes. The Pearson's correlation coefficients observed in *X* and *Y* coordinates of the foveal centers between *AC* and *R* were 0.89 and 0.71 for normal eyes, and 0.88 and 0.86 for AMD eyes, respectively. The differences of *X* and *Y* coordinates between *R* and *AC* for normal eyes and eyes with AMD were higher when compared to intrareader and interreader variability, while the differences are comparable. Figure 11 shows the differences in *X* and *Y* coordinates between the gold standard and the foveal center detected by the automated algorithm, and between the gold standard foveal center and the geometric scan center. In both normal and AMD eyes, the

TABLE I. Mean radial distance measurements of the two observers, each observer at separate sessions, *R*, *SC*, *AC*, ILM algorithm, and ILM-BM algorithm, in both normal eyes and AMD eyes.

	Normal	AMD
Scans/eyes	39/35	58/29
Exp. R11–Exp. R12	29 ± 21	26 ± 33
Exp. R21–Exp. R22	32 ± 19	41 ± 36
Exp. *R*11&*R*12–Exp. *R*21&*R*22	13 ± 24	31 ± 45
SC–R	113 ± 121	139 ± 112
ILM algorithm–R	123 ± 460	260 ± 534
ILM-BM algorithm–R	1889 ± 1074	1713 ± 1083
AC–R	52 ± 56	73 ± 63

ILM algorithm, finding the saliency map of the deepest depression region from the ILM surface; ILM-BM algorithm, searching the smallest distance between ILM and BM. (unit: μm).

differences between the automated method and gold standard were not significantly different in both coordinates (with a *U*-test *P*-value >0.05), while the differences between geometric scan center and gold standard were significantly different (with $P < 0.05$) in the *Y* coordinate and not significantly different (with $P > 0.05$) in the *X* coordinate.

In our image dataset, only 24 advanced AMD scans had original data in Cirrus format. Thus, these raw data with advanced AMD were accessible to be interpreted by a commerically available software package that also estimated the foveal center location (Cirrus review software) and were selected for comparison to results produced by our algorithm. The mean radial distances between our proposed method and the gold standard in these scans (99 ± 83 μm) were much smaller than those between Cirrus and the gold standard (502 ± 1057 μm). These differences between the proposed method and gold standard were not significant ($P > 0.05$), while they were significant for the Cirrus software ($P < 0.05$). In these scans, the correlation observed in the *X* and *Y* coordinates of the foveal center locations between our method and the gold standard (all with Pearson's correlation coefficient $cc > 0.80$) were higher than those between Cirrus and the gold standard (all with Pearson's correlation coefficient $cc < 0.30$).

We also analyzed the central macular retinal thickness by using the Early Treatment Diabetic Retinopathy Study (ETDRS) regions,[4] as centered considering the location determined by *R*, *AC*, and *SC*. Mean and standard deviation retinal thickness measurements for each of the nine standard subfields are shown in Fig. 12. As expected, subfield
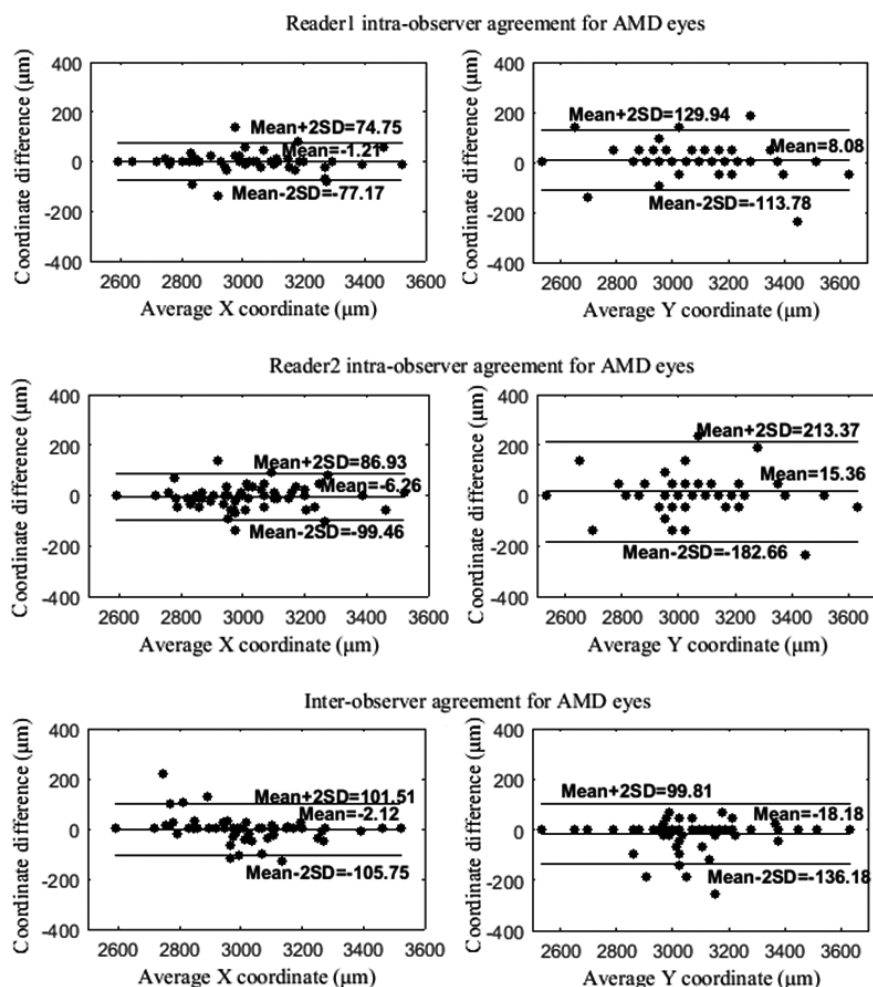

FIG. 9. Bland–Altman plots of intraobserver and interobserver agreement for AMD eyes, where the top, middle, and bottom horizontal lines are Mean+2SD, Mean, and Mean-2SD, respectively. The first and second columns display the Bland–Altman plots for the *X* and *Y* center coordinates, respectively.
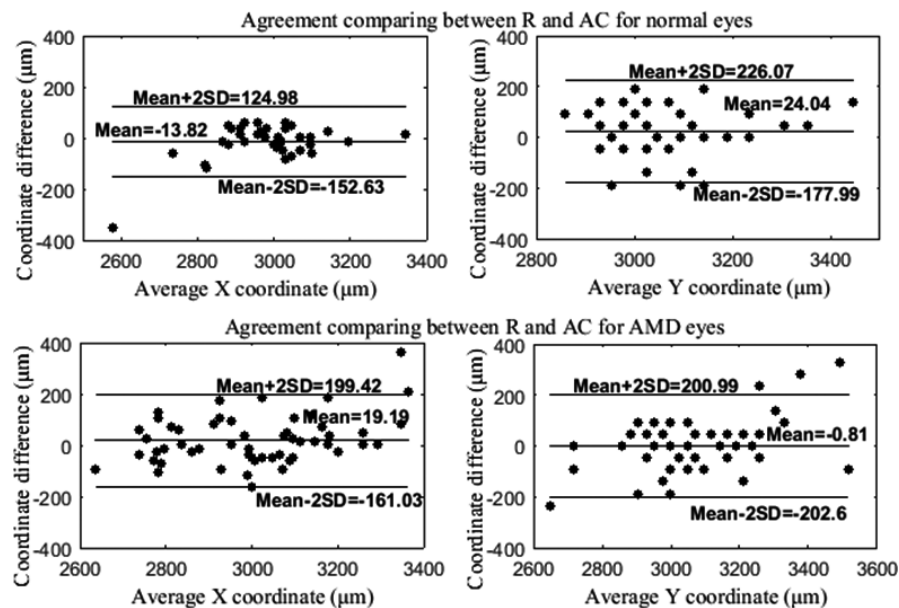
FIG. 10. Bland–Altman plots comparing *R* and *AC* for healthy eyes (first row) and AMD eyes (second row). The first and second columns display the Bland–Altman plots for the *X* and *Y* center coordinates, respectively.
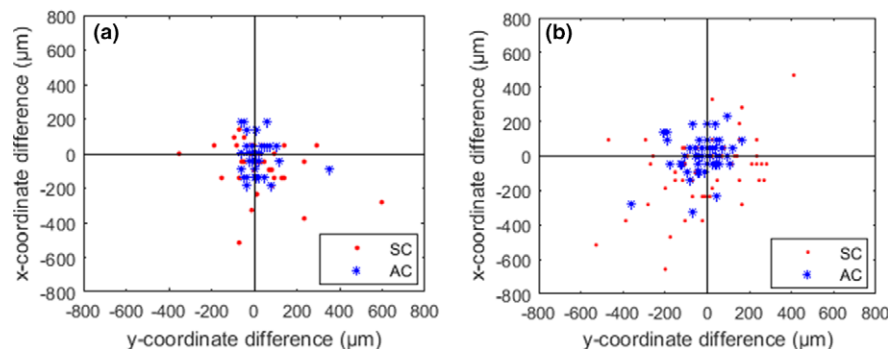

FIG. 11. The distribution of differences between automated method (*AC*) and manual gold standard and image center (*SC*) with gold standard (*R*). The difference of *X* coordinate between *AC* and *R* are computed using X_{AC}-X_R, the difference of *Y* coordinate between *AC* and *R* are computed using Y_{AC}-Y_R. The units are in μm. [Color figure can be viewed at wileyonlinelibrary.com]

thickness measurements are sensitive to the differences in the determination of the foveal center, but to a limited extent given the large regions used to compute an average value. In both normal and AMD eyes, all subfield thickness differences between *AC* and *R* were not statistically significant ($P > 0.05$), while the differences between *SC* and *R* were statistically significant ($P < 0.05$) for the central fovea location and not significant ($P > 0.05$) for the rest of the locations. This result highlights the importance of accurate foveal center determination when computing average thickness in the central fovea region.

4. DISCUSSIONS

During retinal image acquisition, centering the scan at the macular foveal region depends on the patient's cooperation

and their ability to maintain visual fixation, as well as the SD-OCT operator's judgment. As a result of the eye's movement or the operator's misjudgment, the foveal center detected by the OCT acquisition device may deviate from the true foveal center, which may cause an imprecise measurement of central macular thickness. Using an automated postdetection method of the foveal center can reduce the dependency on the participant's cooperation and the SD-OCT operator's judgment. Previous studies[18,19,44] have demonstrated the value of automated foveal center detection algorithms, indicating that the true foveal center produces a proper more precise and reproducible thickness map. In this paper, we propose an automated postdetection method of the foveal center in SD-OCT images.

The mean radial distance between our method and gold standard (52 μm) was lower than that between the geometric
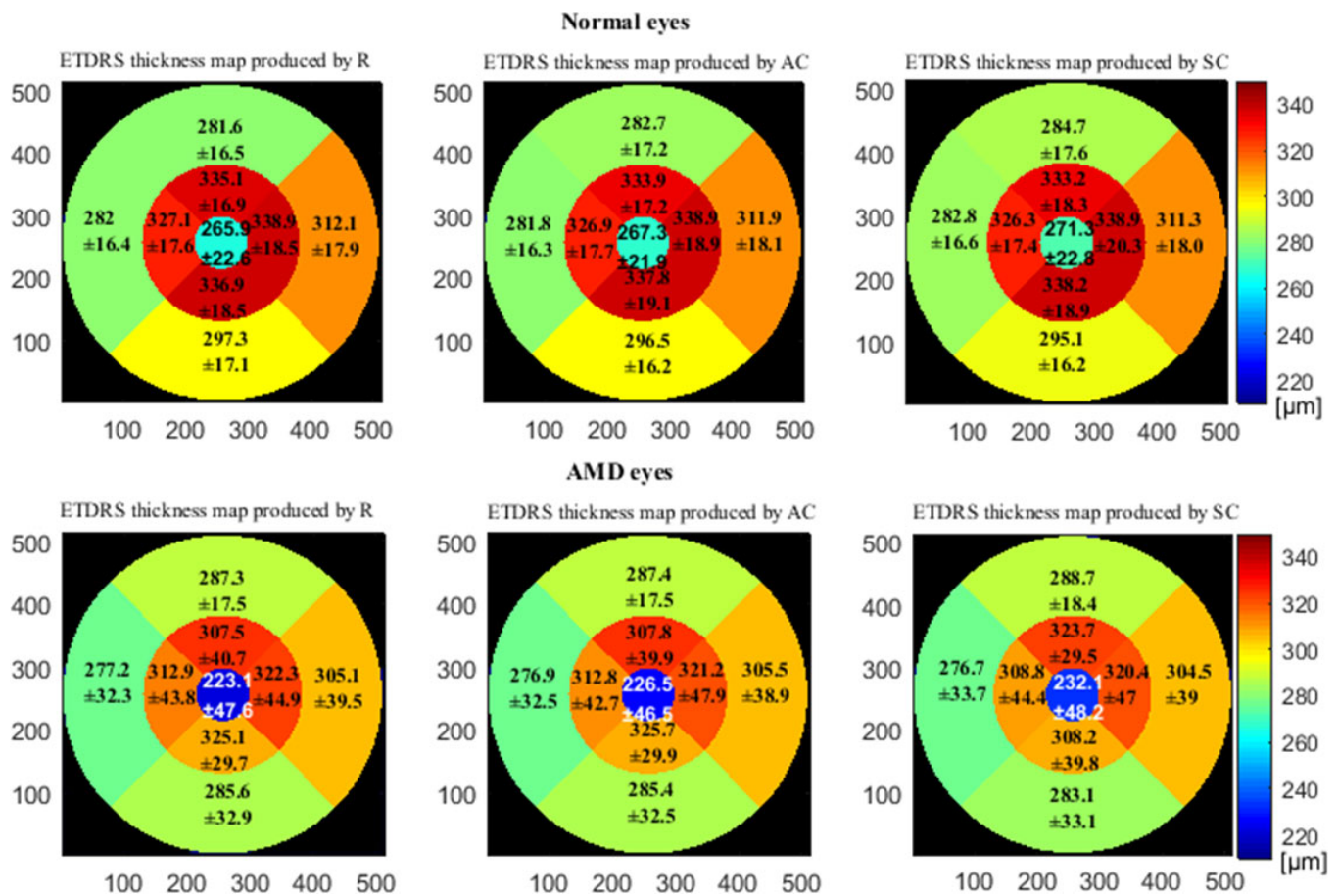
FIG. 12. Macular retinal thickness measurements using Early Treatment Diabetic Retinopathy Study[4] (ETDRS) centered on the foveal center as determined by the manual gold standard (R), our proposed method (AC) and the scanning center (SC) for both normal and AMD eyes. [Color figure can be viewed at wileyonlinelibrary.com]

center and gold standard (113 μm) for the healthy eye scans. For the eyes with AMD, the differences for both automatically detected foveal center and geometric scan center were relatively larger, with mean radial distances increasing to 73 and 139 μm for the automated foveal center and the scan center, respectively. These effects can be also observed in Fig. 11. The larger differences and radial distances in the AMD cases may be due to the presence of large lesions that may change the structure of retinal layers and cause difficulties to determine the foveal center accurately and consistently. On the other hand, the foveal center locations that were estimated using the Cirrus HD-OCT software presented higher errors, causing the mean radial distance between Cirrus and the gold standard to become larger.

In practice, the foveal center is usually identified as the lowest point of ILM, whereas the proposed algorithm also included analysis of the salient of retinal thickness map to identify the foveal depression. The foveal depression is more clearly identified in salient thickness maps than only analyzing the ILM surface, which makes its detection more accurate. As a separate analysis and comparison, we also used the proposed saliency map detection method to identify the foveal center using ILM surface locations instead

of retinal thickness maps, evaluating the same scans included in this work. When compared to the gold standard locations (R), the radial distances (123 ± 460 μm and 260 ± 534 μm for normal and AMD eyes, respectively) were higher than when thickness maps were considered (52 ± 56 μm and 73 ± 63 μm for normal and AMD eyes, respectively, as indicated in Table I). As an additional comparison, we also identified the foveal center by simply searching the smallest distance between ILM and BM. The mean radial distances between the results of this simple method and gold standard (R) in our dataset for both normal and AMD eyes were 1889 ± 1074 μm and 1713 ± 1083 μm (as indicated in Table I), respectively. A comparison of results with the proposed method illustrate that this simple search for the smallest distance between ILM and BM is not as robust. For each scan, all of these methods used the same axial location of the ILM and BM which are estimated by an automated layer segmentation method.[22] We believe the higher accuracy when using the salient of thickness maps may be derived from the fact that although when severe irregularities are present in the ILM and BM surface, the salient of thickness maps between ILM and BM remains relatively robust.
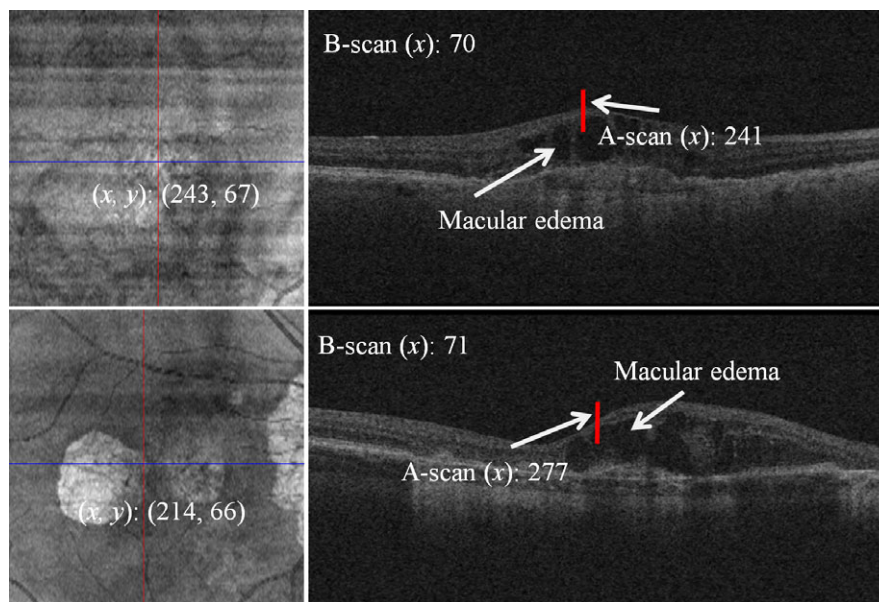
Fig. 13. Results of the automated foveal center detection on examples with macular edema. The positions on the left and right column are determined by gold standard and our method. [Color figure can be viewed at wileyonlinelibrary.com]

Automated detection of the foveal center can improve the accuracy of the retinal thickness measurements compared with the measurements obtained using the geometric scan center, as shown in Fig. 12. Therefore, the automated detection method may provide a more accurate and reliable way to quantify and detect changes in retinal disease. Furthermore, it eliminates the dependence of scan placement at the presumed foveal center during SD-OCT acquisition. Thus, potential errors caused by poor patient cooperation and SD-OCT operator's judgment are reduced or possibly eliminated. The automated detection of the foveal center may also be used to register multimodal retinal images, such as color fundus images (CFIs) and SD-OCT fundus images (SVPIs).

It is important to note that the foveal center identification is a challenge when eyes with significant retinal disease where disruption of retina tissue is present. This effect is due to the lower total retina thickness caused by the macular deformities, such as the presence of severe GA presence, and macular edema. Two cases with diabetic retinopathy had macular edema were shown in Fig. 13, indicating that the results obtained by our method may deviate the real position. Although the proposed method can estimate the foveal center in OCT images with different server diseases, the performance may be affected by the layers segmentation or the disruption of retina tissue. We plan to include the determination of a set of constraints and weights within our method proposed here to better handle such complicated cases in future work.

5. CONCLUSION

This paper presents a novel algorithm for detecting the foveal center automatically in SD-OCT images using the saliency of the retinal thickness map. Quantitative experimental results demonstrate that the proposed method can achieve good performance for normal and abnormal cases with different severe disruption of the retinal anatomy when compared to a consensus manually detected foveal center. Automated foveal center detection by the proposed method could result in more accurate retinal quantitative analysis in SD-OCT images, such as in the foveal center identification for the advanced AMD eyes (especially in eyes with Geographic Atrophy), in the computation of retinal thickness in ETDRS regions, and in multimodal retinal image registration or fusion. This method also provides an opportunity to place the foveal center of the scan on the true center while reducing the need for patient cooperation in the process or clinician judgment.

CONFLICT OF INTEREST

The authors have no relevant conflicts of interest to disclose.

a)Authors to whom correspondence should be addressed. Electronic mails: chen2qiang@njust.edu.cn, sjniu@hotmail.com.

REFERENCES

1. Michael SI, Oden NL, Scott IU, et al. SCORE Study report 3: study design and baseline characteristics. *Ophthalmol.* 2009;116:1770–1777.

2. Diabetic Retinopathy Clinical Research Network. A randomized trial comparing intravitreal triamcinolone acetonide and focal/grid photocoagulation for diabetic macular edema. *Ophthalmol.* 2008;115:1447–1449.

3. Aiello LP, Beck RW, Bressler NM, et al. Rationale for the diabetic retinopathy clinical research network treatment protocol for center-involved diabetic macular edema. *Ophthalmol.* 2011;118:e5–e14.

4. Early Treatment Diabetic Retinopathy Study Research Group. Photocoagulation for diabetic macular edema: Early Treatment Diabetic Retinopathy Study report number 1. *Arch Ophthalmol.* 1985;103:1796–1806.

5. Sinthanayothin C, Boyce J, Cook H, Williamson T. Automated localization of the optic disc, fovea and retinal blood vessels from digital color fundus images. *Br J Ophthalmol.* 1999;83:902–910.

6. Chutatape O. Fundus foveal localization based on vessel model. In Proc. 28th Annual International Conference of the IEEE EMBS, 2006;4440–4444.

7. Gagnon L, Lalonde M, Beaulieu M, Boucher MC. Procedure to detect anatomical structures in optical fundus images. In Proc. the SPIE Symposium on Medical Imaging, 2001;1218–1225.

8. Li H, Chutatape O. Automated feature extraction in color retinal images by a model based approach. *IEEE Trans Biomed Eng.* 2004;51:246–254.

9. Niemeijer M, Abràmoff MD, Ginneken B. Segmentation of the optic disc, macula and vascular arch in fundus photographs. *IEEE Trans Med Imaging.* 2007;26:116–127.

10. Niemeijer M, Abràmoff MD, Ginneken B. Fast detection of the optic disc and fovea in color fundus photographs. *Med Image Anal.* 2009;13:859–870.

11. Gegundez-Arias ME, Marin D, Bravo JM, Suero A. Locating the fovea center position in digital fundus images using thresholding and feature extraction techniques. *Comput Med Imaging Graph.* 2013;37:386–393.

12. Tobin KW, Chaum E, Govindasamy VP, Karnowski TP. Detection of anatomic structures in human retinal imagery. *IEEE Trans Med Imaging.* 2007;26:1729–1739.

13. Fleming AD, Goatman KA, Philip S, Olson JA, Sharp PF. Automatic detection of retinal anatomy to assist diabetic retinopathy screening. *Phys Med Biol.* 2007;52:331–345.

14. Ying H, Liu JC. Automated localization of macula-fovea area on retina images using blood vessel network topology. In Proc. IEEE ICASSP (International Conference on Acoustics, Speech, Signal Processing), 2010;650–653.

15. Yu H, Barriga S, Agurto C, et al. Fast localization of optic disc and fovea in retinal images for eye disease screening. *IEEE Trans Inf Technol Biomed.* 2012;16:644–657.

16. Chin KS, Trucco E, Tan L, Wilson PJ. Automatic fovea location in retinal images using anatomical priors and vessel density. *Pattern Recogn Lett.* 2013;34:1152–1158.

17. Wang L, Yang B, Chen Y, Zhang X, Orchard J. Improving neural-network classifiers using nearest neighbor partitioning. *IEEE Trans Neural Netw Learn Syst.* 2016;99:1–13.

18. Wang F, Gregori G, Rosenfeld PJ. Automated detection of the foveal center improves SD-OCT measurements of central retinal thickness. *Ophthalmic Surg Lasers Imaging.* 2012;43:S32–S37.

19. Legarreta J, Gregori G, Punjabi O, Kniqhton R, Lalwani G, Puliafito C. Macular thickness measurements in normal eyes using spectral domain optical coherence tomography. *Ophthalmic Surg Lasers Imaging.* 2008;39:S43–S49.

20. Wang F, Xu F, Luo D, et al. Detection of macular foveal by optical coherence tomography and its influence on results of measurement of central retina thickness. *Chin J Ophthalmol.* 2012;48:883–887.

21. Chan A, Duker J, Ko T, Fujimoto J, Schuman J. Normal macular thickness measurements in healthy eyes using Stratus optical coherence tomography. *Arch Ophthalmol.* 2006;123:193–198.

22. Niu S, Chen Q, Sisternes L, Rubin DL, Zhang W, Liu Q. Automated retinal layers segmentation in SD-OCT images using dual-gradient and spatial correlation smoothness constraint. *Comput Biol Med.* 2014;54:116–128.

23. Loduca A, Zhang C, Zelkha R, Shahidi M. Thickness mapping of retinal layers by spectral domain optical coherence tomography. *Am J Ophthalmol.* 2010;150:849–855.

24. Chiu S, Li X, Nicholas P, Toth C, Lzatt J, Farsiu S. Automatic segmentation of seven retinal layers in SDOCT images congruent with expert manual segmentation. *Opt Express.* 2010;18:19413–19428.

25. Wang L, Yang B, Orchard J. Particle swarm optimization using dynamic tournament topology. *Appl Soft Comput.* 2016;48:584–596.

26. Rutishauser U, Walther D, Koch C, Perona P. Is bottom-up attention useful for object recognition? In Proc. CVPR, 2004;37–44.

27. Ninassi A, Le MO, Le CP, Barbba D. Applying visual attention to image quality metric. In Proc. IEEE International Conference on Image Processing, 2007;169–172.

28. Itti L, Koch C, Niebur E. A model of saliency-based visual attention for rapid scene analysis. *IEEE Trans Pattern Recog Mach Intell.* 1998;20:1254–1259.

29. Han J, Ngan K, Li M, Zhang H. Unsupervised extraction of visual attention objects in color images. *IEEE Trans Circuits Syst Video Technol.* 2006;16:141–145.

30. Donoser M, Urschler M, Hirzer M, Bischof H. Saliency driven total variation segmentation. In Proc. IEEE ICCV, 2009;817–824.

31. Harel J, Koch C, Perona P. Graph-based visual saliency. In Proc. advances in neural information processing systems, 2007;545–552.

32. Hou X, Zhang L. Saliency detection: a spectral residual approach. In Proc. IEEE Conference on Computer Vision and Pattern Recognition (CVPR), 2007;1–8.

33. Zhang L, Tong M, Marks T, Shan H, Cottrell G. SUN: a Bayesian framework for saliency using natural statistics. *J Vis.* 2008;8:1–20.

34. Xie Y, Lu H, Yang M. Bayesian saliency via low and mid-level cues. *IEEE Trans Image Process.* 2013;22:1689–1698.

35. Cheng M, Zhang G, Mitra NJ, Huang X, Hu S. Global contrast based salient region detection. In Proc. IEEE Conference on Computer Vision and Pattern Recognition (CVPR), 2011;409–416.

36. Liu R, Cao J, Lin Z, Shan S. Adaptive partial differential equation learning for visual saliency detection. In Proc. IEEE Conference on Computer Vision and Pattern Recognition (CVPR), 2014;3866–3873.

37. Seo H, Milanfar P. Nonparametric bottom-up saliency detection by self-resemblance. In Proc. IEEE Conference on Computer Vision and Pattern Recognition Workshops (CVPR), 2009;45–52.

38. Seo H, Milanfar P. Static and space-time visual saliency detection by self-resemblance. *J Vis.* 2009;9:1–27.

39. Greenspan H, Belongie S, Goodman R, Perona P, Rakshit S, Anderson CH. Overcomplete steerable pyramid filters and rotation invariance. In Proc. IEEE Computer Society Conference on Computer Vision and Pattern Recognition (CVPR), 1994;222–228.

40. Brox T, Rosenhahn B, Cremers H. Nonparametric density estimation with adaptive anisotropic kernels for human motion tracking. In Proc. Workshop on Human Motion, Springer-Verlag Berlin Heidelberg (LNCS), 2007;152–165.

41. Vincent P, Bengio Y. Manifold parzen windows. *Adv Neural Inf Process Syst.* 2003;15:825–832.

42. Seo H, Milanfar P. Training-free, generic object detection using locally adaptive regression kernels. *IEEE Trans Pattern Anal Mach Intell.* 2009;32:1688–1704.

43. Fu Y, Yan S, Huang TS. Correlation metric for generalized feature extraction. *IEEE Trans Pattern Anal Mach Intell.* 2008;30:2229–2235.

44. Lujan B, Wang F, Gregori G, et al. Calibration of fundus images using spectral domain optical coherence tomography. *Ophthalmic Surg Lasers Imaging.* 2008;39:S15–S20.

45. Bland J, Altman D. Statistical methods for assessing agreement between two methods of clinical measurement. *Lancet.* 1986;327:307–310.